

Northern High-Latitude Heat Budget Decomposition and Transient Warming

MARIA A. A. RUGENSTEIN

Institute for Marine and Atmospheric Research Utrecht, Utrecht University, Utrecht, Netherlands

MICHAEL WINTON, RONALD J. STOUFFER, STEPHEN M. GRIFFIES, AND ROBERT HALLBERG

NOAA/Geophysical Fluid Dynamics Laboratory, Princeton, New Jersey

(Manuscript received 28 November 2011, in final form 21 June 2012)

ABSTRACT

Climate models simulate a wide range of climate changes at high northern latitudes in response to increased CO₂. They also have substantial disagreement on projected changes of the Atlantic meridional overturning circulation (AMOC). Here, two pairs of closely related climate models are used, with each containing members with large and small AMOC declines to explore the influence of AMOC decline on the high-latitude response to increased CO₂. The models with larger AMOC decline have less high-latitude warming and sea ice decline than their small AMOC decline counterpart. By examining differences in the perturbation heat budget of the 40°–90°N region, it is shown that AMOC decline diminishes the warming by weakening poleward ocean heat transport and increasing the ocean heat uptake. The cooling impact of this AMOC-forced surface heat flux perturbation difference is enhanced by shortwave feedback and diminished by longwave feedback and atmospheric heat transport differences. The magnitude of the AMOC decline within model pairs is positively related to the magnitudes of control climate AMOC and Labrador and Nordic Seas convection. Because the 40°–90°N region accounts for up to 40% of the simulated global ocean heat uptake over 100 yr, the process described here influences the global heat uptake efficiency.

1. Introduction

The ocean damps surface warming in a warming climate by absorbing and storing heat. Increased downward surface heat flux, or ocean heat uptake, influences surface climate change at the global and regional scales. Because of ocean dynamical effects, the resulting ocean heat storage can occur far from the location of heat uptake (Banks and Gregory 2006; Xie and Vallis 2012). Circulation changes redistribute the existing heat content of the ocean in addition to altering the transport of heat away from the surface. The weakening of the Atlantic meridional overturning circulation (AMOC) is a potentially large circulation change affecting the ocean heat transport to high northern latitudes. Projected weakening of the AMOC over the twenty-first century ranges from 0% to more than 50% (Meehl et al. 2007), so its influence on climate is also very uncertain. While

the amplification of Arctic/sub-Arctic atmospheric temperature increase compared to the global mean is a robust feature in models and observations (e.g., Manabe and Stouffer 1979; Hansen et al. 2010), its strength and the causal mechanisms are far from certain. Intermodel correlations (e.g., Holland and Bitz 2003) and heat budgets (Winton 2006) have been used to identify a number of factors that contribute to the uncertainty, such as model differences in cloud cover, ocean heat transport, sea ice state in the control climate, atmospheric heat transport convergence, surface albedo feedback, and other short wave forcings. Separating the different factors is a challenging diagnostic task, even in model simulations where all fields are perfectly known. Multimodel approaches are confounded by the limited number of models and the large number of potential differences between them.

In this study, we make a careful comparison of a few models with limited differences in an attempt to identify the role of a specific process, AMOC weakening, on the simulation of Arctic/sub-Arctic climate change. To the extent the AMOC weakening is influential, it will contribute uncertainty to the high-latitude response. Our

Corresponding author address: Dr. Michael Winton, NOAA/GFDL, Princeton University Forrestal Campus, 201 Forrestal Rd., Princeton, NJ 08540.
E-mail: michael.winton@noaa.gov

TABLE 1. Model components. SIS = Sea Ice Simulator.

	CM2.0	CM2.1	ESM2preG	ESM2G
Atmosphere	AM2 B grid	AM2.1 finite volume	AM2.1 finite volume	AM2.1 finite volume
Ocean	MOM4	MOM4	GOLD	GOLD
Land	LM2	LM2	LM3	LM3
Ice	SIS	SIS	SIS	SIS

approach is complementary to the use of large multi-model ensemble in that we can achieve greater certainty about causal factors but with some risk of losing generality.

We make use of two pairs of models, meaning the two members of each pair are closely related through their formulation. One member of each pair has a large AMOC weakening while the other has a small weakening. Using heat budgets, we trace the influence of the AMOC response differences through their impact on ocean heat transport to intermodel differences in the simulation of ocean heat uptake and the Arctic/sub-Arctic response. We do not attempt to explain the differences in AMOC weakening within our two ensembles. However, we do find that these differences conform to two relationships that have been documented previously. This gives us encouragement that our findings will generalize to larger sets of models.

The first such relationship concerns the AMOC decline and its control climate magnitude. Gregory et al. (2005) show that models with initially stronger AMOCs tend to show an enhanced weakening compared to models with initial weaker AMOCs. The second relationship concerns the role of convection in the Labrador Sea. Weaver et al. (2007) confirmed the results of Gregory et al. (2005) with an intramodel analysis of earth system models of intermediate complexity (EMICs) and found that in cold control climates, freshwater fluxes counteracted AMOC weakening, whereas in warm control climates they enhanced it. The transition took place at the onset of the Labrador Sea convection, which occurs in the model of Weaver et al. (2007) between 240- and 260-ppmv CO₂ forcing. They speculate that the existence of Labrador Sea convection in a model might precondition its transient AMOC response. Gregory (2000) found that, in the northern oceans, reduction in convection was the dominant process leading to deep warming and AMOC weakening.

In our experiments, we will trace this pathway and assess its importance to global ocean heat uptake (OHU). In section 2, the experimental set up and the decomposition of high-latitude heat fluxes are introduced. Section 3 presents the results of the heat budget analysis and some related model features. We discuss the implications of the results in section 4.

2. Models and methods

a. Models

We use two versions of two different atmosphere–ocean coupled general circulation models (AOGCMs). The first pair of climate models is Geophysical Fluid Dynamics Laboratory (GFDL) Climate Model version 2.0 (CM2.0) and CM2.1. These models were used for the Intergovernmental Panel on Climate Change (IPCC) Fourth Assessment Report (AR4) and are fully described by Griffies et al. (2005), Delworth et al. (2006), and Gnanadesikan et al. (2006), with further analyses done by Wittenberg et al. (2006) and Stouffer et al. (2006a). The second pair contains two versions of GFDL's newly developed Earth System Model (ESM2G) described by Dunne et al. (2012). We use ESM2G, which contributes to the phase 5 of the Coupled Model Intercomparison Project (CMIP5) database, as well as a preliminary version, which is referred to here as ESM2preG. A short model description and comparison is given below. The reader is referred to the publications already mentioned for further details.

Table 1 gives an overview of the different climate models and their components. CM2.0 and CM2.1 share the same land model and sea ice model. Likewise, ESM2G and ESM2preG use the same land and sea ice models, although the land model is updated from the earlier version used in CM2.0/CM2.1 and the sea ice model albedos in the ESM models have been set to more physically appropriate values. The ocean model configurations in CM2.0 and CM2.1 differ in the lateral subgrid-scale parameterizations for friction and neutral diffusion, with the CM2.1 settings leading to a stronger subpolar gyre circulation and poleward ocean heat transport. CM2.0 and CM2.1 use different atmospheric dynamical cores, with CM2.0 using the B-grid core from Anderson et al. (2004), whereas CM2.1 uses the finite volume core of Lin (2004). ESM2G and ESM2preG use very nearly the same atmospheric model as CM2.1, and all models use an atmospheric resolution nominally around 2°. The two ESMs share the land model as well, but ESM2G has a 20% reduced total biomass due to another land-vegetation tuning. Both ESMs use generalized ocean layer dynamics (GOLD) with four bulk mixed and buffer layers and 59 interior isopycnal layers

(Dunne et al. 2012). The major differences between the two ESMs are the introduction of geothermal heating and increased diapycnal mixing (i.e., across isopycnal surfaces) in ESM2G compared to ESM2preG, with both added to address a cool drift in the deep ocean of ESM2preG. Since ESM2preG and ESM2G use the same atmospheric component, we can attribute their perturbation differences to one model component, the ocean. All four models use approximately 1° (refined in equatorial areas) grid resolution for the ocean and sea ice models.

b. Experiments

We report on two integrations of each model. The first experiment is a “mean climate” or control run with 1860 forcing. Atmospheric CO₂ concentrations are held constant at 286 ppm. The second experiment includes a forcing of 1% CO₂-concentration increase in the atmosphere each year beginning in year 1860 from the initial condition prescribed by the control experiment. This idealized scenario is a standard to compare model behavior (Manabe et al. 1991; Meehl et al. 2000). We do not aim for predictions of the future real-world climate state and do not discuss the realism of our results in detail. Nonetheless, the 1% CO₂ forcing is linearly transferable to prevalent nonintervention scenario projections (Knutti and Tomassini 2008). The CO₂ mixing ratio quadruples from 286 to 1144 ppm in year 140 and then stays constant. Non-CO₂ forcing agents are held constant at their 1860 values.

To minimize the effect of intrinsic model internal climate variability and seasonality, we always average over the first 100 yr of each run. The pertinent variables obtained by averaging are robust features of the climate system. Since radiative forcing, temperature, and sea ice responses are approximately linear in time (Gregory and Forster 2008; Winton 2008), all variables can be multiplied by 1.4 (=70 yr/50 yr) to obtain an equivalent transient response for the variable at the time of doubling CO₂ around year 70. We use the expressions “response” or “perturbation” to express the difference between the transient forced and the control integration. The assumption is that, if there is a climate drift in the control run, it is present in the forced run with the same strength and makes no contribution to the differences between the two runs. In the following, we do not deal with equilibrium states but exclusively with transient responses.

c. Heat budget decomposition

To analyze the atmospheric and oceanic temperature increase and the amplification of high-latitude temperature increase in particular, we decompose the heat budget into the processes schematically shown in Fig. 1. The region between 40° and 90°N is evaluated, including

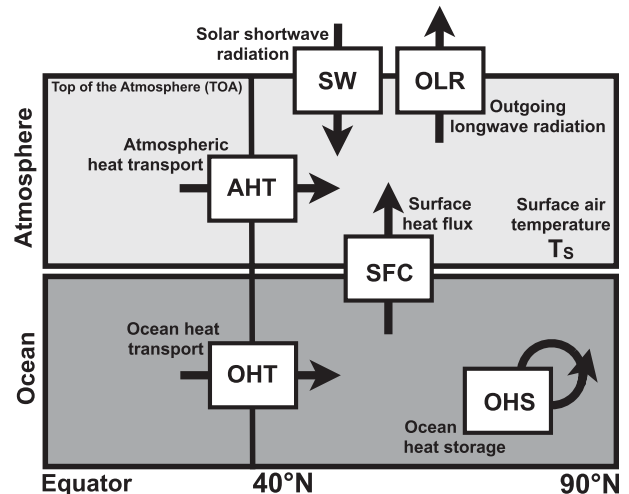


FIG. 1. Processes associated with high-latitude heat budget.

the Arctic and a broad sub-Arctic region. We choose the lower bound of 40°N because the net poleward energy transport and the control climate AMOC strength are largest there (e.g., Trenberth and Caron 2001; Mayer and Haimberger 2011). In addition, in section 3 it will become clear that across our models the decrease of the AMOC, the associated decrease in ocean northward heat transport, and the intramodel variability of the same have a maximum at 35°–40°N. Furthermore the zonal atmospheric vertical temperature response shows a pattern with different regimes north and south of roughly 40°N (Stouffer et al. 2006a; Meehl et al. 2007, their Fig. 10.7). Namely, south of 40°N the upper-tropospheric warming is largest, whereas north of 40°N the surface temperature increase is most pronounced and larger than the global mean. Winton (2006) shows that, although the temperatures of the sub-Arctic regions show only a slightly amplified temperature response relative to the global mean, the standard deviation to mean warming between CMIP3 models is nearly the same as for the Arctic region, indicating that the AOGCMs struggle in representing the sub-Arctic region in the same way as they do in representing the Arctic region.

The absorbed shortwave radiation (SW) and outgoing longwave radiation (OLR) can be differenced to obtain the net downward top-of-atmosphere (TOA) radiation flux. Equation (1) displays the net downward surface heat flux (SFC), or OHU, in the notation of Peixoto and Oort (1992), where $F_{\text{sw}}^{\uparrow\downarrow}$ is the net surface shortwave radiation flux, $F_{\text{lw}}^{\uparrow\downarrow}$ is the net surface longwave radiation flux, $F_{\text{sh}}^{\uparrow\downarrow}$ is the net surface sensible heat flux, F_{lh} is the latent heat flux resulting from evaporation, and F_M is the latent heat flux resulting from melting snow,

$$F_{\text{sfc}}^{\uparrow\downarrow} = F_{\text{sw}}^{\uparrow\downarrow} + F_{\text{lw}}^{\uparrow\downarrow} - F_{\text{sh}}^{\uparrow\downarrow} - F_{\text{lh}} - F_M \quad (1)$$

Throughout our analysis heat fluxes contain latent components. Increased downward surface heat flux is ocean heat uptake and both terms are used throughout the paper. The convergence of atmospheric heat transport ($-\nabla \cdot \text{AHT}$) through 40°N is approximated as the residual of net surface and TOA fluxes: that is, $F_{\text{sfc}}^{\uparrow\downarrow}$ and $F_{\text{TOA}}^{\uparrow\downarrow}$, respectively. We diagnose it assuming the atmosphere has no heat capacity,

$$\frac{dE_A}{dt} = F_{\text{TOA}}^{\uparrow\downarrow} - F_{\text{sfc}}^{\uparrow\downarrow} - \nabla \cdot \text{AHT} \approx 0. \quad (2)$$

The ocean heat transport (OHT) through 40°N includes the effect of large-scale advection resolved by the model and parameterized subgrid-scale, mesoscale, and submesoscale eddy transport. The subgrid parameterizations and bottom and top boundary conditions are formulated differently for each model (Griffies et al. 2005; Delworth et al. 2006; Gnanadesikan et al. 2006; Dunne et al. 2012). The ocean heat storage (OHS) is calculated as the volume integral of $\rho_o c_p \theta$ for the ocean model, where $\rho_o = 1035 \text{ kg m}^{-3}$ is the reference density for the Boussinesq approximation, $c_p = 3992 \text{ J kg}^{-1} \text{ }^{\circ}\text{C}^{-1}$ is the specific heat capacity for seawater, and θ is the potential temperature. The ocean heat transport and perturbation in ocean heat storage are then divided by the earth's surface area between 40° and 90°N in order to compare it to the units of the other fluxes (W m^{-2}). We note that the method for calculating the storage is approximate because averaged temperatures are used to represent the boundaries of the averaging interval. This accounts for the small differences between the divergence of boundary fluxes and estimated heat storage evident in Fig. 2 (as well as in Fig. 7).

Our heat budget analysis accounts for the zonally averaged 40°–90°N polar cap. However, features such as the slowdown of the overturning circulation or the perturbation of surface heat fluxes are most pronounced in the North Atlantic. Unless otherwise noted our analyses are 40°–90°N polar cap means dominated by the North Atlantic signal, which we do not show separately. Similar heat budget studies have been performed using CMIP3 models (e.g., Winton 2008; Lu and Cai 2009) or observations (e.g., Trenberth and Stepaniak 2004).

3. Model comparison

Figure 2a depicts the processes shown in Fig. 1 in the form of the average control-run fluxes of the four models. The atmospheric contribution of the northward energy transport is 5 times greater than the oceanic contribution. The ocean heat storage is close to zero, reflecting a near-equilibrium state. The average surface flux between 40° and 90°N is 9.9 W m^{-2} and directed

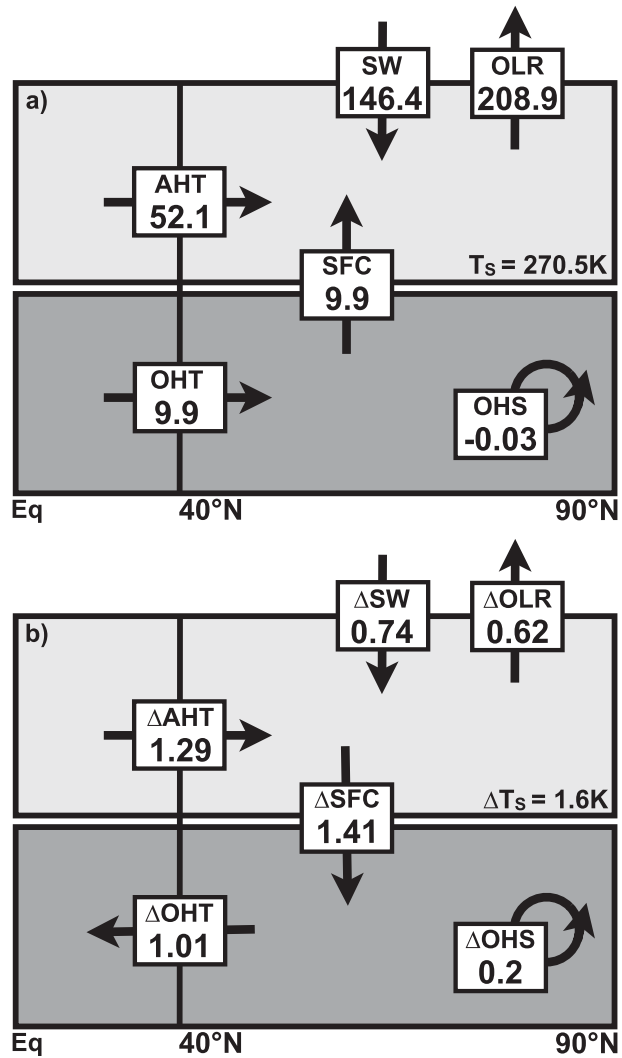


FIG. 2. (a) Mean fluxes of our four models in their control climate state. (b) Mean flux perturbations for the same models (1% $\text{CO}_2 \text{ yr}^{-1}$ forced minus control run) under 2.5 W m^{-2} global CO_2 forcing. All fluxes are in W m^{-2} where the area is the earth's surface between 40° and 90°N. The sum of the fluxes in the atmospheric and oceanic box is only close to zero because the mean of four models is shown. For each individual model they are balanced (not shown). Abbreviations are defined in Fig. 1.

from the ocean to the atmosphere. The OLR balances the overall northward heat transport, surface, and absorbed shortwave fluxes. The simulated and observed partitioning of heat fluxes are similar: Trenberth and Caron (2001) estimate the atmospheric heat transport at 43°N to account for 78% of the net transport and our model mean accounts for 83% in good agreement. Through 40°N our models' control-climate ocean heat transport ranges from 0.6 to 1 PW (not shown), while Trenberth and Caron (2001) report estimates of 0.5–1.2 PW. For a detailed evaluation of our four models

against observations, we refer to Stouffer et al. (2006a), Delworth et al. (2006), Gnanadesikan et al. (2006), and Dunne et al. (2012).

Figure 2b shows the model average response to the forcing: that is, the difference between perturbed and control runs. The high-latitude surface air temperature T_s between 40° and 90°N increases on average by 1.6 K, while the global-mean surface air temperature rise is 1.1 K under an average 2.5 W m^{-2} global CO_2 radiative forcing. To put the high-latitude temperature rise into a multimodel context, we mention that our model mean warming amplification of the more widely used 60° – 90°N region over the global mean, referred to as Arctic amplification, is 2.02. Winton (2006) reports on a 12-model mean Arctic amplification of 1.81. Figure 2b shows furthermore that increases in SW flux and the atmospheric heat transport enhance the warming, while the OLR and the surface heat flux perturbations damp it. The atmospheric heat transport increase is explained by Held and Soden (2006) as a response of latent heat transport to warming. Zelinka and Hartmann (2011) discuss a pathway by which feedbacks pronounced in low latitudes impact and enhance the meridional poleward heat transport and can affect the energy budget at remote places. We show later that atmospheric heat convergence also balances the energy fluxes in the high-latitude region.

All four of our models agree on the sign of the flux perturbations (not shown). The surface heat flux, upward in the controls (i.e., ocean to atmosphere), is reduced by 1.41 W m^{-2} and must be balanced by changes in ocean heat storage (increased by 0.2 W m^{-2}) and ocean heat transport (reduced by 1.01 W m^{-2}). Therefore, the storage accounts for about a fifth of the surface flux perturbation.

Figure 3 shows the perturbed-climate AMOC responses of each model. The annual maximum value of the meridional volume transport, vertically integrated between the surface and the bottom at 40°N (Sv ; $1 \text{ Sv} = 10^6 \text{ m}^3 \text{ s}^{-1}$), was calculated in depth space for the ESM2preG/G models and includes subgrid-scale mixing parameterization (Gent and McWilliams 1990) for CM2.0 and CM2.1. The AMOC loses strength linearly in time until year 140, when CO_2 is capped at quadrupling. The AMOC recovers slightly when CO_2 concentrations are held constant beyond the year 140 of the model integration (for details on CM2.0 and CM2.1 integrations, see Stouffer et al. 2006a). We note that the linearity of the overturning decline over the first century supports our use of averages over this century in our analysis. The fact that models with a strong overturning in the control run, CM2.1 and ESM2G (solid), show a bigger overturning reduction than models with initially weaker overturning,

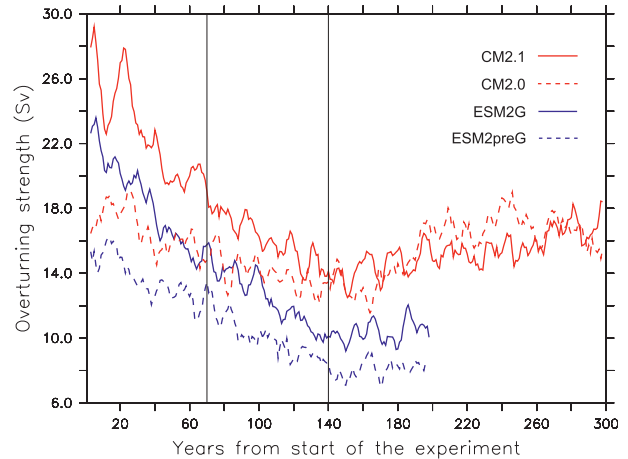


FIG. 3. Time series of the simulated maximum North Atlantic meridional overturning circulation strength at 40°N of the $1\% \text{ CO}_2 \text{ yr}^{-1}$ forced run (Sv ; 5-yr running mean; detailed description in section 3). The time of CO_2 doubling and quadrupling are indicated in years 70 and 140, respectively.

CM2.0 and ESM2preG (dashed), is consistent with the relationship found by Gregory et al. (2005). The relative magnitudes of our AMOC reduction under CO_2 forcing is in the range of the models analyzed by Gregory et al. (2005) (see their Fig. 3): The correlation coefficient of initial AMOC strength and AMOC strength reduction is 0.7 for our four models, 0.74 for AOGCMs and EMICs analyzed by Gregory et al. (2005), 0.63 in EMICs analyzed by Levermann et al. (2007), and 0.87 in the intra-model analysis of one EMIC by Weaver et al. (2007). The ordinary least squares linear regression is calculated with the AMOC reduction at the time of CO_2 quadrupling as the dependent variable and the control climate AMOC strength as the independent variable, both in Sverdrups. The corresponding slope of our models is -0.66 , with the models used by Gregory et al. (2005) having a value of -0.45 . Although our correlation and regression are derived from just four models, the relationships between control overturning and overturning response in the small ensemble studied here confirm the relationships in larger ensembles studied previously.

The impact of the control overturning strength and the overturning decline is expected to be evident in poleward heat transport, with stronger heat transport reduction in models with stronger overturning decline. Figure 4 illustrates the perturbation of the zonally integrated annual-mean ocean northward heat transport. The differences in the control-run North Atlantic heat transport (not shown) reflect the different initial AMOC strengths, with CM2.1 and ESM2G having the stronger and CM2.0 and ESM2preG having the weaker ocean heat transport and AMOC through 40°N . Averaging the

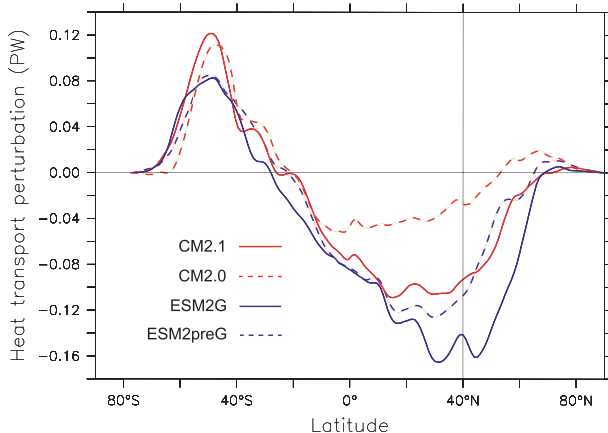


FIG. 4. Zonally integrated perturbation of oceanic northward heat transport (PW). Perturbation means the difference between the 100-yr-averaged $1\% \text{ CO}_2 \text{ yr}^{-1}$ forced and control runs. The vertical black line indicates the lower boundary used for the analysis of the high-latitude heat budget.

perturbation of the four models at 40°N gives the OHT arrow in Fig. 2b. The heat transport perturbation is particularly variable among models around 40°N . Models with a stronger control climate AMOC and a stronger overturning decline (CM2.1 and ESM2G: solid) show a stronger reduction of northward heat transport relative to their weaker overturning counterparts (CM2.0 and ESM2preG: dashed).

a. AMOC decline and Labrador Sea convection

Figure 5 shows the average wintertime mixed layer depths, which can be used as a measure of convection and is defined as the depth where the buoyancy difference with respect to the surface level is greater than or equal to $3 \times 10^{-4} \text{ m s}^{-2}$ (Stouffer et al. 2006a). The top four panels show the control run of each model, corresponding to Fig. 2a, while the bottom four panels show the responses to CO_2 forcing, corresponding to Fig. 2b. Only the North Atlantic is depicted for its most pronounced convective sites. The mixed-layer depths are reduced almost everywhere upon CO_2 forcing; however, focusing on the small-scale details of the top panels of Fig. 5, it is shown that the models differ strongly in strength and location of their northern convective sites. To simplify the reasoning we concentrate on the relative differences inside each model pair. The control-climate wintertime Labrador Sea convection is a prominent difference: CM2.0 and ESM2preG on the left-hand side have very little or no Labrador Sea convection, while CM2.1 and ESM2G show deeper mixed-layer depths (i.e., stronger convection). The bottom panels of Fig. 5 demonstrate that in the Labrador Sea only the models with control-climate convection experience a reduction

of the convection. Other convective areas, such as south of Svalbard and Iceland, show the same magnitude of mixed layer depth perturbation and relation between the models inside each pair.

We confirm the findings of Wood et al. (1999), Stouffer et al. (2006a), and Weaver et al. (2007), who point out that the behavior of the AMOC decline strongly depends on the reduction of the Labrador Sea convection if the model control runs have it. Since in reality there is convection in the Labrador Sea, with disputed impact on the AMOC (Pickart and Spall 2007; Schott et al. 2009), CM2.1 and ESM2G are more realistic regarding the convection than their counterpart models. Comparing Figs. 5 and 3 indicates that initially deeper North Atlantic mixed-layer depths and strong Labrador and Nordic Seas convection is associated with an initially stronger AMOC and a stronger AMOC decline.

b. Transient climate response

The general picture of the temperature response due to increased radiative forcing becomes clear in Fig. 6, which shows the global zonal averages of air and water temperature response for each model. The most robust features are the overall warming of the troposphere with maxima in the low-latitude upper troposphere and at the northern high-latitude surface, as well as the warming of the ocean surface layers. A $50^\circ\text{--}70^\circ\text{N}$ surface and deep-ocean cooling is most pronounced in ESM2G, which experiences the strongest decline in overturning and thereby the strongest heat transport reduction (cf. also Figs. 3, 4). While the ocean heat storage is discussed below, we note here that the cooling deep-ocean volume around 70°N apparent in all four models is relatively small compared to the warming upper-ocean volume around 40°N . A strong upper-ocean warming feature around 70°N is noticeable in CM2.0 and ESM2preG, which have a weak decline of both the AMOC and Labrador Sea convection. The intermodel differences in the ocean warming are more pronounced than in the atmosphere.

The hemispheric asymmetry of the atmospheric temperature increase is a robust feature of climate models (e.g., Manabe and Stouffer 1979; Stouffer et al. 2006a) and observations (e.g., Hansen et al. 2010). The high-latitude atmospheric warming is less in the Southern Hemisphere than in the Northern Hemisphere (NH) across all four models. The smaller land fraction, stronger deep vertical mixing in the Southern Ocean, high altitude of Antarctica, and isolation due to stronger westerly winds are reasons for the smaller Southern Hemispheric warming (Bryan et al. 1988; Flato et al. 2004; Lu and Cai 2009; Masson-Delmotte et al. 2006). Between 90°S and 40°N , the warming responses resemble each other and differ only in the extent of low-latitude upper-tropospheric

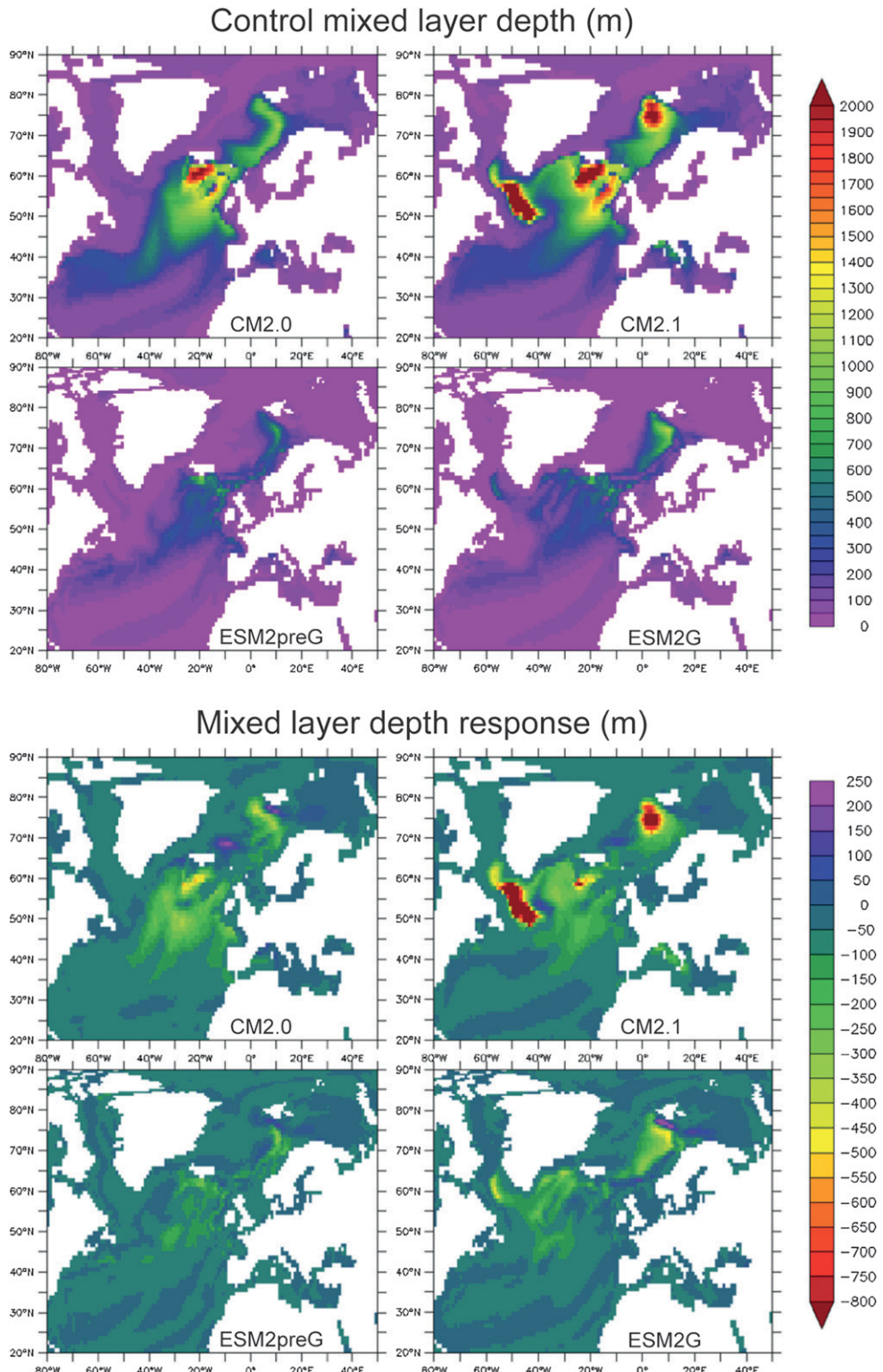


FIG. 5. North Atlantic closeup of the 100-yr-averaged wintertime (January–March) mixed-layer depth (m) for (top four panels) the control climate and (bottom four panels) the perturbation ($1\% \text{CO}_2 \text{ yr}^{-1}$ forced minus control run; different color coding) as a measure of convection. The Labrador Sea convection is only reduced in the models with substantial control-climate Labrador Sea convection.

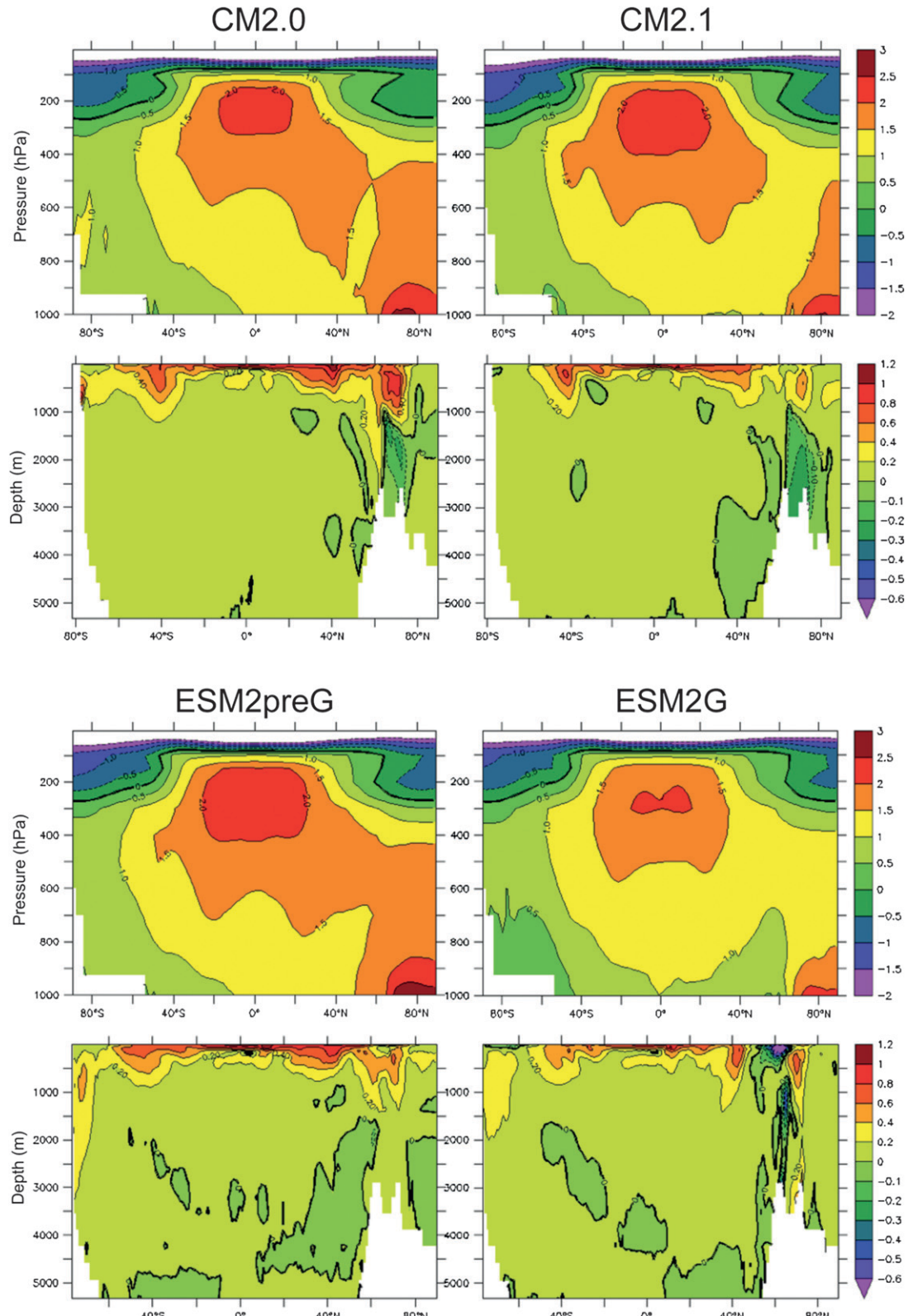


FIG. 6. Zonal-mean atmosphere and ocean temperature perturbation ($1\text{ CO}_2 \text{ yr}^{-1}$ forced minus control run; K) for (top left) CM2.0, (bottom left) ESM2preG, (top right) CM2.1, and (bottom right) ESM2G. The two models on the (right), CM2.1 and ESM2G, are the ones with strong AMOC decline and reduction of Labrador Sea convection.

TABLE 2. Sensitivities of the models using 100-yr-averaged differences of the 1% $\text{CO}_2 \text{ yr}^{-1}$ forced and control run. As discussed in section 2b, one can multiply all entries by 1.4 to approximate the widely used transient response. In the bottom row AMOC is the total North Atlantic meridional volume transport (Sv) at 40°N of the forced-run initial state (before the arrow) and around the year 140 (after the arrow); the percentage reduction is given in parentheses. Single entries and abbreviations are defined and discussed in section 3b.

	Unit	CM2.0	CM2.1	ESM2preG	ESM2G
Global, 40°–90°N ΔT_s	K	1.163, 1.915	1.058, 1.578	1.181, 1.896	0.834, 1.137
Global OHU	W m^{-2}	0.756	0.816	0.86	0.821
Global OHU efficiency	$\text{W m}^{-2} \text{ K}^{-1}$	0.650	0.771	0.728	0.984
40°–90°N, 90°S–40°N OHU efficiency	PW K^{-1}	0.051, 0.269	0.127, 0.276	0.120, 0.259	0.213, 0.296
NH ice reduction efficiency	$10^{12} \text{ m}^2 \text{ K}^{-1}$	−1.468	−1.342	−1.694	−0.851
Initial → reduced AMOC	Sv	17 → 13 (24%)	26 → 14 (46%)	15 → 8 (47%)	22 → 10 (55%)

warming and the vertical pattern of the Southern Hemispheric warming. However, between 40° and 90°N the tropospheric warming responses of the four models differ considerably. CM2.0 and ESM2preG show more extensive northern high-latitude warming and more pronounced hemispheric asymmetry than CM2.1 and ESM2G. Recalling the discussion on convection in section 3a, this means that the models with the more realistic North Atlantic convection pattern show reduced high-latitude atmospheric warming, which agrees less well with observations (Hansen et al. 2010).

Averages of Fig. 6 features are summarized in Table 2. All entries are, like the temperature fields in Fig. 6, the differences of the 100-yr-averaged perturbed climate and the corresponding 100-yr-averaged control climate, as described in section 2b. We are concerned with the large-scale responses: that is, the model differences cover the whole 40°–90°N region. Again, assuming a roughly linear change of climate elements, such as temperature or sea ice retreat, one can multiply all entries by 1.4 to approximate the widely used transient response of the same variables (e.g., Gregory and Forster 2008; Winton 2008). The transient climate response (TCR) is defined as the global-mean surface air temperature response at the time of doubled CO_2 in a model simulation with 1% CO_2 increase per year: that is, a 20-yr average centered around year 70 from the beginning of the perturbed run. Since the AOGCM is not in equilibrium at CO_2 doubling, the TCR depends on the ocean heat uptake as well as the equilibrium climate sensitivity.

The global- and 40°–90°N-average surface air temperature increases are shown in the first row of Table 2. Each model pair has one member (referred to in the following as the more sensitive model) with a large atmospheric temperature and small ocean overturning response and one less sensitive member with a smaller temperature and larger ocean overturning response. The globally more sensitive members also experience a stronger increase of northern high-latitude temperatures. The global ocean heat uptake shown in the second row is the

change in TOA or surface heat flux; that is, we assume the atmosphere has no heat capacity and the overall global heat transport convergence is zero (section 2c). The ocean heat uptake efficiency, meaning the ocean heat uptake normalized with the surface temperature increase, was introduced as a proportionality constant to relate the TCR linearly to the ocean heat uptake by Gregory and Mitchell (1997). The global ocean heat uptake efficiency is smaller in each pair's more sensitive model (CM2.0 and ESM2preG) compared to its comparatively less sensitive counterpart (CM2.1 and ESM2G).

Here, the regional ocean heat uptake efficiency is calculated using the change in surface fluxes. To account for the northern high latitudes, the fourth row shows that the 40°–90°N region takes up a substantial amount of heat compared with the remaining 90°S–40°N. The heat uptake and heat uptake efficiency in the 40°–90°N region ranges from 16% (in CM2.0) to 41% (in ESM2G) of the global value. Previous work emphasized the impact of the Southern Ocean dynamics on the global heat uptake (Stouffer et al. 2006b). Here, we emphasize the role of the North Atlantic. Its share of global ocean heat uptake efficiency is large enough to be important to the global efficiency differences.

The next-to-last row shows that the reduced warming in CM2.1 and ESM2G is also reflected in a smaller efficiency of the reduction in northern sea ice extent (the ice cover reduction per degree of global warming). Winton (2011) discusses intermodel variations in this metric for IPCC AR4 models. In the Labrador Sea (not shown), the sea ice cover is reduced in the more sensitive model of each pair, CM2.0 and ESM2preG, while it increases slightly in the less sensitive models, CM2.1 and ESM2G.

Finally, the last row confirms Gregory et al. (2005) and summarizes Fig. 3 in describing the reduction of the annual-mean maximum AMOC strength at 40°N for its initial strength (averaged over years 1–10; Sv), its strength at CO_2 quadrupling (averaged over years 130–150; Sv), and the reduction in percentage. In summary, the second and fourth columns show that the models

with the strong control overturning and strong overturning decline, as well as a reduction of Labrador and Nordic Seas convection, are the ones with higher ocean heat uptake efficiency, smaller high-latitude temperature amplification, and a smaller sea ice extent reduction efficiency compared to their counterpart models.

c. High-latitude temperature amplification

In Fig. 7, we use the same region as in Figs. 2a,b. Here the energy budget displays the difference of flux perturbations for each model pair,

$$\Delta\Delta F = (\Delta F)_{\text{more sensitive model}} - (\Delta F)_{\text{less sensitive model}},$$

where F is any of the fluxes or the heat storage depicted in Fig. 1, the more sensitive models are CM2.0 and ESM2preG with a stronger surface temperature increase, and the less-sensitive models are CM2.1 and ESM2G with a weaker surface temperature increase. In other words, Fig. 7 shows the flux perturbation (ΔF) differences (Δ) of each model pair. As an example the ocean heat transport reduction of 1.03 W m^{-2} through 40°N in CM2.1 is subtracted from the ocean heat transport reduction of 0.28 W m^{-2} in CM2.0. Thus, the reduction in ocean heat transport in CM2.0 is 0.75 smaller than in CM2.1, and the OHT difference arrow in Fig. 7a points north.

The main idea is to determine the cause of the temperature response differences. In both cases the enhanced temperature increase between 40° and 90°N is forced by the surface heat flux perturbation difference and amplified by the TOA SW perturbation difference. Both are marked by arrows pointing into the atmospheric part of the high-latitude box in Figs. 7a,b. On the other hand the atmospheric heat transport, as well as the OLR flux differences, reflecting the difference in surface temperature, damps the temperature response differences, which is indicated by arrows pointing outward. The difference in surface heat flux perturbation is consistent with the difference in oceanic heat transport perturbation, since the differences in heat storage between the models are very small (0.02 and 0.004 W m^{-2}). The response of the overturning circulation and associated change in ocean heat transport are hence important elements of high-latitude climate change. Bitz et al. (2006) and Winton (2008) discuss a reverse pathway by which ice albedo feedback impacts ocean circulation. However, this pathway, which has an albedo reduction driving an overturning reduction, is counter to the model differences shown here, since a larger albedo reduction was associated with larger ocean heat uptake in these studies. It should be mentioned further that, although the TOA SW and OLR perturbation differences have the same sign

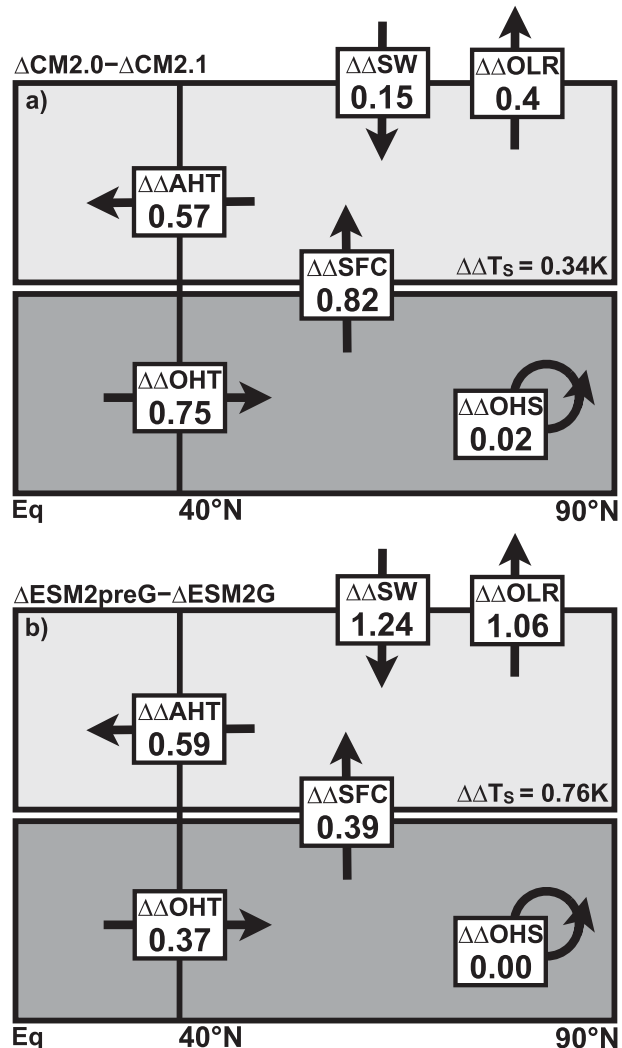


FIG. 7. Forcing of the difference in 100-yr-averaged northern high-latitude temperature perturbation: that is, $1\% \text{ CO}_2 \text{ yr}^{-1}$ forced minus control run. (a) $\Delta CM2.0 - \Delta CM2.1$, (b) $\Delta ESM2preG - \Delta ESM2G$. Fluxes are described in W m^{-2} where the area is the earth's surface between 40° and 90°N .

for both model pairs, the net TOA radiation, $\Delta\Delta SW - \Delta\Delta OLR$, is negative for $\Delta CM2.0 - \Delta CM2.1$ but positive for $\Delta ESM2preG - \Delta ESM2G$.

4. Discussion and concluding remarks

We have shown the surface heat flux response to radiative forcing to be important for the high-latitude temperature amplification. Since the difference of ocean heat storage responses between our model pairs turns out to be negligible, it is the difference in northward heat transport responses that accounts for the difference in surface flux perturbation. In turn, the difference in ocean heat transport between the models is consistent

with the magnitude of decreasing strength of the AMOC and the associated decreasing convection in the Labrador and Nordic Seas.

With the Labrador Sea convection, we have identified a small-scale ocean dynamical mechanism that influences the heat uptake at Northern Hemispheric high latitudes (Wood et al. 1999; Weaver et al. 2007). This result confirms earlier findings that ocean dynamics plays a crucial role in heat uptake (Banks and Gregory 2006; Xie and Vallis 2012). In addition, the Labrador Sea convection is a feature of the control climate that is important to the magnitude of AMOC response and hemispheric warming asymmetry (Stouffer et al. 2006a).

Table 2 and Fig. 4 indicate that our models show a larger high-latitude temperature amplification with initially weaker overturning and thus weaker northward heat transport reduction (CM2.0 and ESM2G) than their initially strong overturning counterparts (CM2.1 and ESM2G). This result is in contrast to the model analysis of Mahlstein and Knutti (2011), which suggests that models with an initially weaker ocean heat transport (in their case through 60°N; cf. our Fig. 4) would show less high-latitude temperature amplification. We confirm the finding of Levermann et al. (2007) that models with initially weaker overturning experience a smaller surface heat flux response than their initially strong overturning counterparts. They argue that enhanced ocean heat loss would allow for more convection and thus stabilize the AMOC decrease. Counter to the EMIC analysis of Levermann et al. (2007), the high-latitude oceans in our models do not show enhanced ocean heat loss or enhanced convection. Instead, they show enhanced heat uptake and reduced convection (see section 3). The same relationship is also valid for the 60°–90°N region (not shown here) used by Levermann et al. (2007). Both Mahlstein and Knutti (2011) and Levermann et al. (2007) use the surface albedo feedback (SAF) as the central point in their line of argumentation, either to explain the Arctic amplification or to explain the oceanic convection response and AMOC decrease.

To assess the importance of the SAF relative to the surface heat flux perturbation, we analyze the TOA SW perturbation in detail (as, e.g., Hall 2004; Graversen and Wang 2009). As described in Winton (2006), we separate the effect of the SAF and the non-SAF on the TOA SW perturbation. The analysis reveals that the model mean TOA SW perturbation is driven by the SAF-induced enhanced ocean shortwave heat uptake and damped by non-SAF (atmospheric) processes.

Table 3 shows a TOA SW breakdown, which clarifies that, in terms of high-latitude temperature increase amplification, the non-SAF might act to reduce the temperature amplification difference (in the comparison

TABLE 3. TOA SW perturbation over the 40°–90°N region and perturbation differences split into the SAF and non-SAF contributions (W m^{-2}). Net TOA is positive downward and perturbation means the 100-yr-averaged difference of the 1% $\text{CO}_2 \text{ yr}^{-1}$ forced and control runs.

	Net TOA SW	= SAF + non-SAF
$\Delta\text{CM2.0} - \Delta\text{CM2.1}$ (Fig. 7a)	0.15	= 0.38 – 0.23
$\Delta\text{ESM2preG} - \Delta\text{ESM2G}$ (Fig. 7b)	1.24	= 0.84 + 0.4

of the CMs) or enhance it (in the comparison of the ESMs). As also shown by Hall (2004), we conclude that the SAF should be used with caution in causal explanations of the high-latitude temperature increase amplification and the AMOC reduction behavior. The models with larger SAF reductions had smaller AMOC reductions. Since the differences in surface heat flux can drive as well as be driven by the differences in AMOC response, we cannot determine causality. However, the formulation of the ESM2preG/G pair, with only the ocean mixing being substantially different, indicates an oceanic driver as a possible explanation for the differences. This is a rare opportunity to trace a significant change in sensitivities to formulation differences between the model components.

In section 3c and Fig. 7, we showed our model high-latitude surface warming difference to be forced by the difference in surface heat flux perturbation and amplified by the differences in TOA SW SAF-induced perturbation. Atmospheric heat transport and the OLR differences act to damp the high-latitude temperature amplification, while the non-SAF contribution of the TOA SW perturbation might act either to damp or to enhance differences.

Our results on the importance of the Labrador Sea convection may be sensitive to resolution because the Labrador Sea itself is only marginally resolved with the 1° ocean models used here. The distance between Cape Farewell and Newfoundland spans only 12 grid cells in our models (see Fig. 5 and also section 2b). The real-world Labrador Sea convection is influenced by baroclinic eddies that form along the western Greenland coast and enable restratification. According to Jourdain et al. (2010), either a $1/15^\circ$ resolution or extremely accurate eddy parameterizations is needed to describe the Labrador Sea convection appropriately.

The fact that our two models with more realistic Labrador Sea convection do show less-realistic high-latitude atmospheric warming calls for in-depth modeling studies to determine causal physical mechanisms. We suggest further investigation with high-resolution eddy-resolving ocean and climate models to represent

the coupled interactions of sea ice and ocean circulation that remain to be understood in detail.

Acknowledgments. We thank the developers of Geophysical Fluid Dynamics Laboratory models used here and gratefully acknowledge Isaac Held, Thomas Delworth, Reto Knutti, and three anonymous reviewers for comments on the manuscript.

REFERENCES

- Anderson, J. L., and Coauthors, 2004: The new GFDL global atmosphere and land model AM2/LM2: Evaluation with prescribed SST simulations. *J. Climate*, **17**, 4641–4673.
- Banks, H. T., and J. M. Gregory, 2006: Mechanisms of ocean heat uptake in a coupled climate model and the implications for tracer based predictions of ocean heat uptake. *Geophys. Res. Lett.*, **33**, L07608, doi:10.1029/2005GL025352.
- Bitz, C. M., P. R. Gent, R. A. Woodgate, M. M. Holland, and R. Lindsay, 2006: The influence of sea ice on ocean heat uptake in response to increasing CO₂. *J. Climate*, **19**, 2437–2450.
- Bryan, K., S. Manabe, and M. J. Spelman, 1988: Interhemispheric Asymmetry in the transient response of a coupled ocean-atmosphere model to CO₂ forcing. *J. Phys. Oceanogr.*, **18**, 851–867.
- Delworth, T. L., and Coauthors, 2006: GFDL's CM2 global coupled climate models. Part I: Formulation and simulation characteristics. *J. Climate*, **19**, 643–674.
- Dunne, J. P., and Coauthors, 2012: GFDL's ESM2 global coupled climate–carbon Earth system models. Part I: Physical formulation and baseline simulation characteristics. *J. Climate*, **25**, 6646–6665.
- Flato, G. M., and Coauthors, 2004: Sea-ice and its response to CO₂ forcing as simulated by global climate models. *Climate Dyn.*, **23**, 229–241, doi:10.1007/s00382-004-0436-7.
- Gent, P. R., and J. C. McWilliams, 1990: Isopycnal mixing in ocean circulation models. *J. Phys. Oceanogr.*, **20**, 150–155.
- Gnanadesikan, A., and Coauthors, 2006: GFDL's CM2 global coupled climate models. Part II: The baseline ocean simulation. *J. Climate*, **19**, 675–697.
- Graversen, R. G., and M. Wang, 2009: Polar amplification in a coupled climate model with locked albedo. *Climate Dyn.*, **33**, 629–643.
- Gregory, J. M., 2000: Vertical heat transports in the ocean and their effect on time-dependent climate change. *Climate Dyn.*, **16**, 501–515, doi:10.1007/s003820000059.
- , and J. F. B. Mitchell, 1997: The climate response to CO₂ of the Hadley Centre coupled AOGCM with and without flux adjustment. *Geophys. Res. Lett.*, **24**, 1943–1946.
- , and P. M. Forster, 2008: Transient climate response estimated from radiative forcing and observed temperature change. *J. Geophys. Res.*, **113**, D23105, doi:10.1029/2008JD010405.
- , and Coauthors, 2005: A model intercomparison of changes in the Atlantic thermohaline circulation in response to increasing atmospheric CO₂ concentration. *Geophys. Res. Lett.*, **32**, L12703, doi:10.1029/2005GL023209.
- Griffies, S. M., and Coauthors, 2005: Formulation of an ocean model for global climate simulations. *Ocean Sci.*, **1**, 45–79.
- Hall, A., 2004: The role of surface albedo feedback in climate. *J. Climate*, **17**, 1550–1568.
- Hansen, J., R. Ruedy, M. Sato, and K. Lo, 2010: Global surface temperature change. *Rev. Geophys.*, **48**, RG4004, doi:10.1029/2010RG000345.
- Held, I. M., and B. J. Soden, 2006: Robust responses of the hydrological cycle to global warming. *J. Climate*, **19**, 5686–5699.
- Holland, M., and C. Bitz, 2003: Polar amplification of climate change in coupled models. *Climate Dyn.*, **21**, 221–232.
- Jourdain, N. C., B. Barnier, J. Molines, J. Chanut, N. Ferry, G. Garric, and L. Parent, 2010: Deep convection in the Labrador Sea, as captured by a global ocean reanalysis and regional downscaling. *Extended Abstracts, Fall Meeting*, San Francisco, CA, Amer. Geophys. Union, OS54B-07.
- Knutti, R., and L. Tomassini, 2008: Constraints on the transient climate response from observed global temperature and ocean heat uptake. *Geophys. Res. Lett.*, **35**, L09701, doi:10.1029/2007GL032904.
- Levermann, A., J. Mignot, S. Nawarath, and S. Rahmstorf, 2007: The role of northern sea ice cover for the weakening of the thermohaline circulation under global warming. *J. Climate*, **20**, 4160–4171.
- Lin, S. J., 2004: A “vertically Lagrangian” finite-volume dynamical core for global models. *Mon. Wea. Rev.*, **132**, 2293–2307.
- Lu, J., and M. Cai, 2009: Seasonality of polar surface warming amplification in climate simulations. *Geophys. Res. Lett.*, **36**, L16704, doi:10.1029/2009GL040133.
- Mahlstein, I., and R. Knutti, 2011: Ocean heat transport as a cause for model uncertainty in projected Arctic warming. *J. Climate*, **24**, 1451–1460.
- Manabe, S., and R. J. Stouffer, 1979: A CO₂-climate sensitivity study with a mathematical model of the global climate. *Nature*, **282**, 491–493.
- , —, M. J. Spelman, and K. Bryan, 1991: Transient responses of a coupled ocean atmosphere model to gradual changes of atmospheric CO₂. Part I: Annual mean response. *J. Climate*, **4**, 785–818.
- Masson-Delmotte, V., and Coauthors, 2006: Past and future polar amplification of climate change: Climate model intercomparisons and ice-core constraints. *Climate Dyn.*, **26**, 513–529, doi:10.1007/s00382-005-0081-9.
- Mayer, M., and L. Haimberger, 2011: Poleward atmospheric energy transports and their variability as evaluated from ECMWF reanalysis data. *J. Climate*, **25**, 734–752.
- Meehl, G. A., G. J. Boer, C. Covey, M. Latif, and R. J. Stouffer, 2000: The Coupled Model Intercomparison Project (CMIP). *Bull. Amer. Meteor. Soc.*, **81**, 313–318.
- , and Coauthors, 2007: Global climate projections. *Climate Change 2007: The Physical Science Basis*, S. Solomon et al., Eds., Cambridge University Press, 747–846.
- Peixoto, J., and A. Oort, Eds., 1992: *Physics of Climate*. American Institute of Physics, 520 pp.
- Pickart, R. S., and M. A. Spall, 2007: Impact of Labrador Sea convection on the North Atlantic meridional overturning circulation. *J. Phys. Oceanogr.*, **37**, 2207–2227.
- Schott, F. A., L. Stramma, B. S. Giese, and R. Zantopp, 2009: Labrador Sea convection and subpolar North Atlantic Deep Water export in the SODA assimilation model. *Deep-Sea Res. I*, **56**, 926–938, doi:10.1016/j.dsr.2009.01.001.
- Stouffer, R. J., and Coauthors, 2006a: GFDL's CM2 global coupled climate models. Part IV: Idealized climate response. *J. Climate*, **19**, 723–740.
- , J. Russel, and M. J. Spelman, 2006b: Importance of oceanic heat uptake in transient climate change. *Geophys. Res. Lett.*, **33**, L17704, doi:10.1029/2006GL027242.

- Trenberth, K. E., and J. M. Caron, 2001: Estimates of meridional atmosphere and ocean heat transports. *J. Climate*, **14**, 3433–3443.
- , and D. P. Stepaniak, 2004: The flow of energy through the earth's climate system. *Quart. J. Roy. Meteor. Soc.*, **130**, 2677–2701.
- Weaver, A. J., E. Michael, M. Kienast, and O. A. Saenko, 2007: Response of the Atlantic meridional overturning circulation to increasing atmospheric CO₂: Sensitivity to mean climate state. *Geophys. Res. Lett.*, **34**, L05708, doi:10.1029/2006GL028756.
- Winton, M., 2006: Amplified Arctic climate change: What does surface albedo feedback have to do with it? *Geophys. Res. Lett.*, **33**, L03701, doi:10.1029/2005GL025244.
- , 2008: Sea ice–albedo feedback and nonlinear Arctic climate change. *Arctic Sea Ice Decline: Observations, Projections, Mechanisms, and Implications, Geophys. Monogr.*, Vol. 180, Amer. Geophys. Union, 111–131.
- , 2011: Do climate models underestimate the sensitivity of Northern Hemisphere sea ice cover? *J. Climate*, **24**, 3924–3934.
- Wittenberg, A. T., A. Rosati, N.-C. Lau, and J. J. Poshay, 2006: GFDL's CM2 global coupled climate models. Part III: Tropical Pacific climate and ENSO. *J. Climate*, **19**, 698–722.
- Wood, R. A., A. B. Keen, J. F. B. Mitchell, and J. M. Gregory, 1999: Changing spatial structure of the thermohaline circulation in response to atmospheric CO₂ forcing in a climate model. *Nature*, **399**, 572–575.
- Xie, P., and G. Vallis, 2012: The passive and active nature of ocean heat uptake in idealized climate change experiments. *Climate Dyn.*, **38**, 667–684, doi:10.1007/s00382-011-1063-8.
- Zelinka, M. D., and D. L. Hartmann, 2011: Climate feedbacks and their implications for poleward energy flux changes in a warming climate. *J. Climate*, **25**, 608–624.